Monthly Notices of the ROYAL ASTRONOMICAL SOCIETY

MNRAS **530,** 3240–3251 (2024) https://doi.org/10.1093/mnras/stae1106
Advance Access publication 2024 April 24

WISDOM Project – XIX. Figures of merit for supermassive black hole mass measurements using molecular gas and/or megamaser kinematics

Hengyue Zhang [1]★ Martin Bureau,[1]★ Mark D. Smith [1] Michele Cappellari [1] Timothy A. Davis [2] Pandora Dominiak [1] Jacob S. Elford [2] Fu-Heng Liang [1] Ilaria Ruffa [2,3] and Thomas G. Williams [1]

[1]*Sub-department of Astrophysics, Department of Physics, University of Oxford, Denys Wilkinson Building, Keble Road, Oxford OX1 3RH, UK*
[2]*School of Physics & Astronomy, Cardiff University, Queens Buildings, The Parade, Cardiff CF24 3AA, UK*
[3]*INAF - Istituto di Radioastronomia, via P. Gobetti 101, I-40129 Bologna, Italy*

Accepted 2024 April 22. Received 2024 April 22; in original form 2024 February 14

ABSTRACT

The mass ($M_{\rm BH}$) of a supermassive black hole (SMBH) can be measured using spatially resolved kinematics of the region where the SMBH dominates gravitationally. The most reliable measurements are those that resolve the smallest physical scales around the SMBHs. We consider here three metrics to compare the physical scales probed by kinematic tracers dominated by rotation: the radius of the innermost detected kinematic tracer $R_{\rm min}$ normalized by the SMBH's Schwarzschild radius ($R_{\rm Schw} \equiv 2GM_{\rm BH}/c^2$, where G is the gravitational constant and c the speed of light), sphere-of-influence (SOI) radius ($R_{\rm SOI} \equiv GM_{\rm BH}/\sigma_{\rm e}^2$, where $\sigma_{\rm e}$ is the stellar velocity dispersion within the galaxy's effective radius), and equality radius [the radius $R_{\rm eq}$ at which the SMBH mass equals the enclosed stellar mass, $M_{\rm BH} = M_*(R_{\rm eq})$, where $M_*(R)$ is the stellar mass enclosed within the radius R]. All metrics lead to analogous simple relations between $R_{\rm min}$ and the highest circular velocity probed $V_{\rm c}$. Adopting these metrics to compare the SMBH mass measurements using molecular gas kinematics to those using megamaser kinematics, we demonstrate that the best molecular gas measurements resolve material that is physically closer to the SMBHs in terms of $R_{\rm Schw}$ but is slightly farther in terms of $R_{\rm SOI}$ and $R_{\rm eq}$. However, molecular gas observations of nearby galaxies using the most extended configurations of the Atacama Large Millimeter/submillimeter Array can resolve the SOI comparably well and thus enable SMBH mass measurements as precise as the best megamaser measurements.

Key words: masers – galaxies: ISM – galaxies: kinematics and dynamics – galaxies: nuclei.

1 INTRODUCTION

Supermassive black hole (SMBH) masses ($M_{\rm BH}$) correlate with several properties of their host galaxies, such as stellar velocity dispersion, bulge mass, and stellar mass (e.g. Magorrian et al. 1998; Ferrarese & Merritt 2000; Gebhardt et al. 2000; Beifiori et al. 2012; Kormendy & Ho 2013). These correlations are sufficiently tight to suggest (potentially self-regulating) co-evolutionary processes, although their exact nature remains unclear (e.g. Kormendy & Ho 2013; Simmons, Smethurst & Lintott 2017; Krajnović, Cappellari & McDermid 2018; Sahu, Graham & Davis 2019).

The mass of an SMBH can be directly measured from observations of a kinematic tracer sufficiently close to it that its contribution to the total galactic gravitational potential can be disentangled from (i.e. is comparable to) the contributions of other constituents (e.g. stars, gas, dust, and/or dark matter). This is simplest when observations resolve the spatial scales on which the SMBH dominates the potential (e.g. Boizelle et al. 2019; North et al. 2019; Ruffa et al. 2023). However, with a reliable model of the distributions of the other mass components, the SMBH's contribution can still be discerned (with commensurately larger uncertainties) by tracing velocities higher than those expected from models with no SMBH (e.g. Davis et al. 2018; Smith et al. 2019). Stars and ionized gas are common kinematic tracers and have yielded most of the published SMBH mass measurements to date. Measurements with megamasers (hereafter 'masers' for short) as tracers are often thought of as the 'gold standard' (e.g. Herrnstein et al. 2005; Kuo et al. 2011, 2020; Gao et al. 2017; Zhao et al. 2018), as very long baseline interferometry (VLBI) allows to resolve very small angular scales (and thus physical scales) close to the SMBHs. However, suitable masers are rare and are detected almost exclusively in galaxies with Seyfert 2 active galactic nuclei (AGNs), hosting SMBHs of relatively low masses ($10^6 \lesssim M_{\rm BH}/{\rm M}_\odot \lesssim 10^8$; e.g. Braatz, Wilson & Henkel 1996; Greenhill et al. 2003; van den Bosch 2016).

More recently, advances in millimetre interferometry have enabled to resolve molecular gas on the spatial scales over which central SMBHs dominate the galactic potentials. Following an initial proof-of-concept measurement in NGC 4526 (Davis et al. 2013), additional measurements have been performed by our millimetre-Wave Interferometric Survey of Dark Object Masses (WISDOM) in 10 typical early-type galaxies (ETGs; Davis et al. 2017, 2018; Onishi et al. 2017; North et al. 2019; Smith et al. 2019, 2021; Ruffa et al. 2023; Dominiak et al. 2024b; Zhang et al. 2024), a dwarf ETG

★ E-mail: hengyue.zhang@physics.ox.ac.uk(HZ); martin.bureau@physics.ox.ac.uk(MB)

(Davis et al. 2020), and a peculiar luminous infrared galaxy with a Seyfert nucleus (Lelli et al. 2022). Using similar techniques, other groups have presented molecular gas SMBH mass measurements of 12 additional ETGs (Barth et al. 2016; Boizelle et al. 2019, 2021; Nagai et al. 2019; Ruffa et al. 2019; Cohn et al. 2021, 2023; Kabasares et al. 2022; Nguyen et al. 2022; Dominiak et al. 2024a) and three late-type galaxies (LTGs), all barred spirals (Onishi et al. 2015; Nguyen et al. 2020, 2021). Although the molecular gas technique is well suited to a range of galaxies, it is more challenging to apply to LTGs because the shallower and occasionally non-axisymmetric potentials make non-circular gas motions more significant (e.g. Combes et al. 2019).

VLBI observations of masers for SMBH mass measurements resolve much smaller physical scales than molecular gas observations. However, the absolute scales do not necessarily offer a meaningful comparison, as the scale required to perform an SMBH mass measurement, the radius of the SMBH's sphere of influence (SOI), is proportional to the SMBH mass. Kormendy & Ho (2013) showed that, among all SMBH measurements published by then, that of NGC 4258 by Herrnstein et al. (2005) using masers had the most resolution elements across the SOI and was thus the most precise extragalactic SMBH mass measurement. North et al. (2019) however demonstrated that, considering instead the number of spatially resolved Schwarzschild radii, their molecular gas observations of NGC 383 resolved spatial scales comparable to those of the maser measurements of the Megamaser Cosmology Project (e.g. Kuo et al. 2011; Gao et al. 2017).

In this paper, we consider three separate metrics that quantify the physical scales probed by kinematic tracers in circular motions: the radius of the innermost detected dynamical tracer divided by the SMBH's Schwarzschild radius $R_{\rm Schw}$, SOI radius $R_{\rm SOI}$ (estimated using the effective stellar velocity dispersion), and equality radius $R_{\rm eq}$ (the radius at which the SMBH mass equals the enclosed stellar mass). We then adopt the metrics to compare the resolved spatial scales of maser and molecular gas dynamical SMBH mass measurements. In Section 2, we introduce the metrics by rewriting the circular velocities $V_{\rm c}(R)$ of the Keplerian circular velocity curves using different $M_{\rm BH}$-independent forms. In Section 3, we estimate and collect the parameters of all existing SMBH mass measurements to date that use molecular gas and/or maser observations. We also compare their minimum resolved spatial scales using the metrics introduced and discuss the results and their implications. We conclude in Section 4.

2 KEPLERIAN CIRCULAR VELOCITY CURVES IN DIFFERENT UNITS

For kinematic tracers dominated by rotation (so primarily molecular gas and masers rather than ionized gas or stars), the key factor for the precision of an SMBH mass measurement (assuming a sufficient signal-to-noise ratio has been achieved) is how well the observations resolve the innermost part of the rotation curve, where the motion is predominantly Keplerian and gravitationally dominated by the SMBH (Davis 2014). In other words, a precise measurement requires observations with a spatial resolution sufficiently high to probe the kinematics very close to the SMBH and deep into its potential well. VLBI maser measurements are thus considered the gold standard of SMBH measurements, as they resolve spatial scales much smaller than those reached by other methods (see e.g. Table 1). However, as argued above, an absolute scale does not necessarily offer a meaningful metric, because the scale required to perform an SMBH mass measurement (the SOI) itself depends on $M_{\rm BH}$. A better spatial resolution will only lead to a more precise $M_{\rm BH}$ measurement at a fixed mass. It is thus more meaningful to compare the spatial scales probed by different kinematic tracers using a set of units that eliminate the $M_{\rm BH}$ dependence. In this section, we thus rewrite the circular velocity $V_{\rm c}(R)$ of Keplerian rotation using three different pairs of such units and introduce three corresponding metrics to compare SMBH mass measurements that use different tracers.

2.1 Natural units (c and $R_{\rm Schw}$)

The velocity of any kinematic tracer in a circular motion due to gravity is such that the gravitational acceleration equals the centrifugal acceleration:

$$\frac{GM(R)}{R^2} = \frac{V_{\rm c}^2}{R}, \tag{1}$$

where G is the gravitational constant, $M(R)$ the mass enclosed within a sphere of radius R, and $V_{\rm c}$ the circular velocity at R. The enclosed mass $M(R)$ includes contributions from all the mass components (SMBH, stars, gas, dust, dark matter, etc). However, for the rest of the discussion, we assume that $M(R)$ in the central region of each galaxy is dominated by the SMBH and the stars, as the gas fraction and the dark matter fraction are usually low in the nuclear regions of local galaxies (e.g. Cappellari et al. 2013; Zhu et al. 2023). We also note that for a non-spherically symmetric mass distribution, mass outside of the radius R also contributes to the kinematics. Those contributions however tend to cancel out, and the net effect is negligible compared to the high circular velocities in the nuclear region. Multiplying both sides of equation (1) by the Schwarzschild radius

$$R_{\rm Schw} \equiv \frac{2GM_{\rm BH}}{c^2} \tag{2}$$

(Schwarzschild 1916), where c is the speed of light, yields

$$\left(\frac{V_{\rm c}}{c}\right)^2 = \frac{1}{2}\left(\frac{R}{R_{\rm Schw}}\right)^{-1}\frac{M(R)}{M_{\rm BH}}. \tag{3}$$

For a tracer much closer to the SMBH than the SOI radius, the BH mass dominates over the stellar mass (i.e. $M(R) \approx M_{\rm BH}$), and

$$\left(\frac{V_{\rm c}}{c}\right)^2 \approx \frac{1}{2}\left(\frac{R}{R_{\rm Schw}}\right)^{-1}. \tag{4}$$

In this manner, we have rewritten the Keplerian relation between $V_{\rm c}$ and R in natural units, eliminating its explicit dependence on the SMBH mass. This approach allows a fair comparison of observations of different kinematic tracers, in terms of the proximity of each tracer to the SMBH in units of the Schwarzschild radius, even when the SMBH masses are different by orders of magnitude. Observations that resolve circumnuclear disc material the fewest Schwarzschild radii away from the SMBH will thus detect the highest rotational velocities and reveal the physical processes of SMBH accretion and feedback closest to the galactic nucleus.

As a caveat, the Keplerian relation in equation (4) is only satisfied by kinematic tracers well within the SOI, so if an observation does not highly resolve the SOI, as is the case for many molecular gas observations (shown later in Section 3.2.4), the velocities of the kinematic tracer are expected to deviate from equation (4). By contrast, most SMBH measurement observations using masers do highly resolve the SOI. The masers are thus expected to closely follow equation (4). This will be discussed in detail in Section 3.2.4.

Table 1. Molecular gas and maser SMBH mass measurements.

Galaxy	Distance (Mpc)	R_{min} (mas)	R_{min} (pc)	V_{max} (km s^{-1})	σ_e (km s^{-1})	Inclination (deg)	log (M_{BH}/M$_\odot$)	R_{SOI} (mas)	R_{eq} (mas)	Reference
Molecular gas measurements										
Fairall 49	86.7 ± 6.1	110 ± 30	46 ± 13	208 ± 15	–	58 ± 3	8.20 ± 0.28	–	280 ± 90	Lelli et al. (2022)
NGC 315	70 ± 7.0	70 ± 30	24 ± 10	532 ± 10	341 ± 7	74.2 ± 0.1	9.32 ± 0.05	230 ± 30	740 ± 70	Boizelle et al. (2021)
NGC 383	66.6 ± 9.9	44 ± 7	14 ± 2	634 ± 20	239 ± 16	38 ± 1	9.55 ± 0.02	840 ± 120	830 ± 20	Zhang et al. (2024)
NGC 404	3.1 ± 0.4	75 ± 35	1.1 ± 0.5	61 ± 2	40 ± 3	37 ± 1	5.74 ± 0.09	100 ± 30	60 ± 10	Davis et al. (2020)
NGC 524	23.3 ± 2.3	480 ± 20	54 ± 2	131 ± 10	220 ± 11	20 ± 5	8.60 ± 0.22	310 ± 160	280 ± 70	Smith et al. (2019)
NGC 997	90.4 ± 9.0	190 ± 30	83 ± 13	162 ± 5	215 ± 10	35 ± 0	8.99 ± 0.25	210 ± 120	250 ± 60	Dominiak et al. (2024a)
NGC 1097	14.5 ± 1.5	1450 ± 250	102 ± 18	210 ± 10	195 ± 4	46 ± 5	8.15 ± 0.10	230 ± 50	530 ± 40	Onishi et al. (2015)
NGC 1275	71 ± 7.1	30 ± 10	10 ± 3	420 ± 20	245 ± 28	46 ± 9	9.04 ± 0.19	230 ± 110	530 ± 120	Nagai et al. (2019)
NGC 1332	22.3 ± 1.9	210 ± 50	31 ± 5	500 ± 20	331 ± 15	84 ± 1	8.82 ± 0.04	240 ± 30	230 ± 10	Barth et al. (2016)
NGC 1380	17.1 ± 1.7	150 ± 30	12 ± 2	270 ± 10	215 ± 8	76.9 ± 0.1	8.17 ± 0.15	170 ± 60	230 ± 50	Kabasares et al. (2022)
NGC 1574	19.3 ± 1.9	60 ± 20	5.6 ± 1.9	120 ± 10	216 ± 16	27 ± 2	8.00 ± 0.08	100 ± 20	190 ± 30	Ruffa et al. (2023)
NGC 1684	62.8 ± 2.3	420 ± 90	128 ± 27	334 ± 10	262 ± 10	66.5 ± 0.4	9.16 ± 0.08	300 ± 60	350 ± 40	Dominiak et al. (2024a)
NGC 3258	31.9 ± 3.9	90 ± 30	14 ± 5	486 ± 10	260 ± 10	49.0 ± 0.1	9.35 ± 0.04	920 ± 100	900 ± 40	Boizelle et al. (2019)
NGC 3504	32.4 ± 2.1	75 ± 35	12 ± 5	148 ± 10	119 ± 10	53 ± 1	7.19 ± 0.05	30 ± 6	58 ± 3	Nguyen et al. (2020)
NGC 3557	43.3 ± 4.3	140 ± 10	29 ± 2	225 ± 22	282 ± 16	56 ± 1	8.85 ± 0.02	180 ± 20	620 ± 10	Ruffa et al. (2019)
NGC 3593	7 ± 2	290 ± 50	9.8 ± 1.7	124 ± 10	55 ± 7	75.0 ± 0.1	6.38 ± 0.08	100 ± 30	90 ± 10	Nguyen et al. (2022)
NGC 3665	34.7 ± 6.8	250 ± 50	42 ± 8	220 ± 10	219 ± 10	69.9 ± 0.2	8.76 ± 0.03	310 ± 40	540 ± 20	Onishi et al. (2017)
NGC 4261	31.1 ± 3.1	65 ± 40	9.8 ± 6.0	582 ± 15	263 ± 12	60.8 ± 0	9.21 ± 0.01	670 ± 60	1140 ± 10	Ruffa et al. (2023)
NGC 4429	16.5 ± 1.6	550 ± 100	44 ± 8	170 ± 10	178 ± 8	66.8 ± 0.1	8.18 ± 0.09	260 ± 60	270 ± 20	Davis et al. (2018)
NGC 4526	16.4 ± 1.8	350 ± 30	28 ± 2	288 ± 10	209 ± 10	79 ± 0	8.65 ± 0.14	550 ± 180	540 ± 100	Davis et al. (2013)
NGC 4697	11.4 ± 1.1	210 ± 30	12 ± 2	230 ± 10	169 ± 8	76 ± 1	8.10 ± 0.02	340 ± 30	410 ± 10	Davis et al. (2017)
NGC 4751	26.9 ± 2.9	210 ± 70	27 ± 9	687 ± 30	355 ± 14	78.6 ± 0.2	9.45 ± 0.04	740 ± 90	460 ± 40	Dominiak et al. (2024b)
NGC 4786	62.1 ± 9.3	170 ± 30	51 ± 9	263 ± 20	264 ± 10	69.3 ± 0.7	8.70 ± 0.14	100 ± 30	220 ± 30	Kabasares et al. (2024)
NGC 5193	45.7 ± 3.2	170 ± 20	38 ± 4	234 ± 10	194 ± 7	60.7 ± 0.1	8.15 ± 0.18	70 ± 30	90 ± 20	Kabasares et al. (2024)
NGC 6861	27.3 ± 4.5	1390 ± 250	184 ± 33	468 ± 20	389 ± 3	72.7 ± 0.1	9.30 ± 0.20	430 ± 200	500 ± 140	Kabasares et al. (2022)
NGC 7052	69.3 ± 5.0	220 ± 20	74 ± 7	382 ± 30	266 ± 13	75 ± 1	9.40 ± 0.02	450 ± 50	580 ± 10	Smith et al. (2021)
NGC 7469	68.4 ± 18.8	160 ± 40	46 ± 13	182 ± 10	152 ± 16	53 ± 1	7.20 ± 0.97	9 ± 8	80 ± 70	Nguyen et al. (2021)
PGC 11 179	89 ± 8.9	210 ± 10	91 ± 4	391 ± 20	266 ± 9	60.0 ± 0.1	9.28 ± 0.09	270 ± 60	140 ± 20	Cohn et al. (2023)
UGC 2698	91 ± 9.1	120 ± 30	53 ± 13	481 ± 20	304 ± 6	68 ± 1	9.39 ± 0.14	260 ± 80	170 ± 30	Cohn et al. (2021)
Maser measurements										
CGCG 074-064	87.6 ± 7.6	0.28 ± 0.01	0.119 ± 0.004	902 ± 3	113 ± 3	91 ± 1	7.38 ± 0.04	24 ± 3	–	Pesce et al. (2020a)
Circinus	2.8 ± 0.5	5.3 ± 0.1	0.072 ± 0.001	260 ± 2	158 ± 18	90 ± 0	6.06 ± 0.08	15 ± 4	–	Greenhill et al. (2003)
ESO 558–G009	107.6 ± 5.9	0.44 ± 0.09	0.23 ± 0.05	575 ± 14	170 ± 20	98 ± 1	7.23 ± 0.03	5 ± 1	–	Gao et al. (2017)
IC 1481	78.7 ± 5.5	7.3 ± 2.7	2.8 ± 1.0	170 ± 6	95 ± 26	90 ± 0	7.11 ± 0.11	16 ± 10	–	Mamyoda et al. (2009)
IC 2560	31 ± 13	1.14 ± 0.17	0.17 ± 0.03	325 ± 20	141 ± 10	90 ± 0	6.62 ± 0.06	6 ± 1	–	Yamauchi et al. (2012)
IRAS 08452-0011	213 ± 15	0.30 ± 0.13	0.31 ± 0.13	832 ± 4	137 ± 11	85.2 ± 0.3	7.52 ± 0.03	7 ± 1	–	Kuo et al. (2020)
J0437+2456	65.3 ± 3.6	0.13 ± 0.08	0.041 ± 0.025	442 ± 11	110 ± 13	81 ± 1	6.46 ± 0.05	3 ± 1	–	Gao et al. (2017)
J1346+5228	121 ± 12	0.22 ± 0.04	0.13 ± 0.02	788 ± 8	139 ± 4	90 ± 0	7.24 ± 0.06	7 ± 1	–	Zhao et al. (2018)
Mrk 1	61.5 ± 2.3	1.48 ± 0.21	0.44 ± 0.06	203 ± 4	86 ± 4	90 ± 2	6.51 ± 0.07	6 ± 1	–	Kuo et al. (2020)
Mrk 1029	120.8 ± 6.6	0.39 ± 0.05	0.23 ± 0.03	163 ± 26	132 ± 15	79 ± 2	6.28 ± 0.12	0.8 ± 0.3	–	Gao et al. (2017)
NGC 1068	15.9 ± 9.4	8.0 ± 0.2	0.62 ± 0.02	330 ± 10	151 ± 7	90 ± 0	6.95 ± 0.02	22 ± 2	–	Lodato & Bertin (2003)
NGC 1194	58.0 ± 6.3	2.17 ± 0.30	0.61 ± 0.08	685 ± 15	148 ± 24	85 ± 0	7.85 ± 0.02	50 ± 20	–	Kuo et al. (2011)
NGC 1320	34.2 ± 1.9	0.38 ± 0.07	0.063 ± 0.012	402 ± 11	141 ± 16	90 ± 0	6.74 ± 0.21	7 ± 4	–	Gao et al. (2017)
NGC 2273	29.5 ± 1.9	0.28 ± 0.05	0.040 ± 0.007	958 ± 15	145 ± 17	84 ± 0	6.93 ± 0.02	12 ± 3	–	Kuo et al. (2011)
NGC 2960	67.1 ± 7.1	0.42 ± 0.06	0.14 ± 0.02	581 ± 15	151 ± 7	89 ± 0	7.03 ± 0.02	6.2 ± 0.6	–	Kuo et al. (2011)

Table 1 – *continued*

Galaxy	Distance (Mpc)	$R_{\rm min}$ (mas)	$R_{\rm min}$ (pc)	$V_{\rm max}$ (km s^{-1})	$\sigma_{\rm e}$ (km s^{-1})	Inclination (deg)	log ($M_{\rm BH}$/M$_\odot$)	$R_{\rm SOI}$ (mas)	$R_{\rm eq}$ (mas)	Reference
NGC 3079	15.9 ± 1.2	4.8 ± 0.4	0.37 ± 0.03	145 ± 25	145 ± 7	84 ± 0	6.36 ± 0.09	6 ± 1	–	Yamauchi et al. (2004)
NGC 3393	49.2 ± 8.2	1.7 ± 0.4	0.41 ± 0.10	575 ± 5	148 ± 10	90 ± 0	7.20 ± 0.32	13 ± 10	–	Kondratko, Greenhill & Moran (2008)
NGC 4258	7.3 ± 0.5	4.5 ± 0.2	0.159 ± 0.007	1001 ± 7	115 ± 11	81 ± 0	7.58 ± 0.01	350 ± 70	244 ± 5	Herrnstein et al. (2005)
NGC 4388	16.5 ± 1.6	2.5 ± 0.2	0.20 ± 0.02	405 ± 3	107 ± 7	90 ± 0	6.86 ± 0.01	34 ± 5	–	Kuo et al. (2011)
NGC 4945	3.7 ± 0.4	9.2 ± 3.8	0.17 ± 0.07	149 ± 4	135 ± 6	90 ± 0	6.14 ± 0.18	18 ± 8	–	Greenhill, Moran & Herrnstein (1997)
NGC 5495	95.7 ± 5.3	0.37 ± 0.15	0.17 ± 0.07	533 ± 67	166 ± 19	95 ± 1	7.04 ± 0.08	4 ± 1	–	Gao et al. (2017)
NGC 5765B	112.2 ± 5.3	0.56 ± 0.03	0.30 ± 0.02	760 ± 3	158 ± 18	72.4 ± 0.5	7.62 ± 0.02	13 ± 3	–	Pesce et al. (2020b)
NGC 6264	132.1 ± 19.3	0.39 ± 0.01	0.250 ± 0.006	729 ± 1	159 ± 15	91 ± 2	7.44 ± 0.06	7 ± 2	–	Pesce et al. (2020b)
NGC 6323	109.4 ± 28.8	0.27 ± 0.02	0.14 ± 0.01	540 ± 2	158 ± 26	91.5 ± 0.3	7.01 ± 0.11	3 ± 1	–	Pesce et al. (2020b)
UGC 3789	51.5 ± 4.3	0.35 ± 0.01	0.087 ± 0.002	847 ± 1	107 ± 12	84.9 ± 0.6	7.08 ± 0.03	18 ± 4	–	Pesce et al. (2020b)
UGC 6093	152 ± 15	0.29 ± 0.05	0.21 ± 0.04	816 ± 13	155 ± 18	94 ± 4	7.41 ± 0.02	6 ± 2	–	Zhao et al. (2018)
Sgr A* (S2)	0.008	1400 $R_{\rm Schw}$	5.5×10^{-4}	7650	105 ± 20	–	6.61 ± 0.01	1.6 pc	3.1 pc	GC18

2.2 Units of σ_e and R_{SOI}

Equations (3) and (4) express V_c and R in natural units, providing a metric that quantifies how well an observation spatially resolves the material and motions in the circumnuclear disc. However, this metric is not ideal for evaluating the reliability of SMBH mass measurements, as the natural units relate only to the SMBH and contain no information on how other components of the gravitational potential compare to it. For example, at a fixed radius in natural units, a kinematic tracer in a galaxy with an overly massive central bulge (compared to its SMBH) will be more affected by stars than one in a galaxy with an undermassive bulge. Everything else being equal, the latter case generally yields a more precise SMBH mass than the former. To evaluate an SMBH mass measurement in units that reflect both the SMBH and the stars, and thus the likely precision of the measurement, we normalize R by the radius of the SMBH SOI

$$R_{SOI} \equiv \frac{GM_{BH}}{\sigma_e^2} \tag{5}$$

(e.g. Wolfe & Burbidge 1970), where σ_e is the stellar velocity dispersion measured within one effective (half-light) radius R_e of the galaxy, a proxy for the depth of the galaxy potential well and thus the stellar component at large spatial scales. The relation between V_c and R then becomes

$$\left(\frac{V_c}{\sigma_e}\right)^2 = \left(\frac{R}{R_{SOI}}\right)^{-1} \frac{M(R)}{M_{BH}}. \tag{6}$$

Again, for $R \ll R_{SOI}$, $M(R) \approx M_{BH}$, and

$$\left(\frac{V_c}{\sigma_e}\right)^2 \approx \left(\frac{R}{R_{SOI}}\right)^{-1}. \tag{7}$$

It is worth noting that when R is normalized by R_{SOI}, V_c is normalized by σ_e. This is reasonable as the SOI is the region where the influence of the SMBH potential exceeds that of the stellar potential. So, for a tracer at R_{SOI}, the SMBH's contribution to the circular velocity should approximately equal the contribution from the stars, which is of the order of σ_e. Again, observations that only marginally resolve the SOI ($R \approx R_{SOI}$) have $M(R)$ considerably larger than M_{BH}, so the velocities are expected to deviate from equation (7).

2.3 Units of V_{eq} and R_{eq}

Although σ_e is measurable for most nearby galaxies and provides a convenient way to estimate the size of the SOI, it is only a proxy for the dynamics of the stars and their underlying gravitational potential. The SOI definition in equation (5) is thus only an approximation to the more physically meaningful definition that the SOI is the region where the SMBH potential dominates over the stellar potential, or equivalently where the SMBH mass dominates over the stellar mass. Therefore, we consider a more formal and accurate definition of the SOI radius, the equality radius R_{eq}, such that

$$M_*(R_{eq}) = M_{BH}\ , \tag{8}$$

where $M_*(R)$ is the stellar mass enclosed within the radius R. We then define V_{eq} to be the circular velocity at R_{eq} due only to the SMBH:

$$V_{eq} \equiv \sqrt{\frac{GM_{BH}}{R_{eq}}}\ . \tag{9}$$

In these units, the relation between V_c and R becomes

$$\left(\frac{V_c}{V_{eq}}\right)^2 = \left(\frac{R}{R_{eq}}\right)^{-1} \frac{M(R)}{M_{BH}}\ . \tag{10}$$

Again, for $R \ll R_{eq}$, $M(R) \approx M_{BH}$, and

$$\left(\frac{V_c}{V_{eq}}\right)^2 \approx \left(\frac{R}{R_{eq}}\right)^{-1}\ . \tag{11}$$

Unlike the definition of R_{SOI} that approximates the comparison between the SMBH and the stellar potential with the comparison between V_c and σ_e, the definition of R_{eq} comes from an explicit comparison between the SMBH mass and the stellar mass distribution. Therefore, V_{eq} and R_{eq} are better physically motivated and more accurate units to compare the depths of the potentials probed by different observations. Having said that, detailed modelling of the stellar mass distribution near the SMBH SOI is not available (nor feasible) for every galaxy with a dynamically measured SMBH mass. This is particularly the case for maser galaxies, as their SOI are often smaller than the angular resolutions of even the best optical telescopes (e.g. *Hubble Space Telescope*, *HST*, and *JWST*; see Section 3.2.4). Hence, V_{eq} and R_{eq} are only available for a subset of the galaxies considered in the next section, and this will be discussed in detail.

3 COMPARING MASER AND MOLECULAR GAS MEASUREMENTS

3.1 Methods

In this section, we compile all molecular gas and maser SMBH mass measurements in the literature and compare them using the metrics introduced in Section 2. Instead of re-deriving the entire rotation curve of each galaxy in the new units, we consider only the radius R_{min} and velocity V_{max} of the innermost kinematic tracer measurement in these units. This reveals the smallest spatial scale probed by each observation and indicates the quality of the mass measurement.

For maser galaxies, we thus adopt the (redshifted or blueshifted) maser spot that has the highest velocity relative to the galaxy's dynamical centre. The uncertainties of the maser position and velocity and those of the dynamical centre position and velocity are taken from the original publication and are added using the standard error propagation procedures for Gaussian random variables.

By contrast, molecular gas observations yield continuous emission distributions in the radius-velocity planes, commonly shown in the literature as major-axis position–velocity diagrams (PVDs). For each galaxy, we thus visually identify the major-axis position (i.e. the radius) with the highest velocity (i.e. the velocity peak) in the central region of the PVD. If the observation resolves the SOI, this velocity traces the velocity rise due to the SMBH. If the SOI is unresolved and no velocity rise is detected, this velocity represents the innermost resolved velocity within which the observed velocity rapidly falls off to zero. In this case, a BH mass measurement is still possible if the velocity is substantially higher than that expected from models of the other mass components only.

In practice, we extract the corresponding radius and velocity using WebPlotDigitizer[1] (Rohatgi 2022). If the redshifted and blueshifted velocity peaks look almost symmetric, we measure both peaks and adopt the average R_{min} and V_{max} of the two measurements, with half of the differences as the uncertainties. If the resulting V_{max} uncertainty is smaller than the channel width of the data cube, we inflate it to the channel width.

[1] https://automeris.io/WebPlotDigitizer/index.html

We note that the channel width is a conservative estimate of the typical uncertainty of velocity measurements from data cubes. If one of the peaks has a substantially lower velocity than the other or is indistinguishable from noise, we adopt the other (higher velocity) peak and estimate the position uncertainty from the spatial width of that peak and the velocity uncertainty as the channel width. We also note that $R_{\rm min}$ is sometimes marginally smaller than the full width at half-maximum (FWHM) of the synthesized beam of the observations, as the position of the central unresolved emission can be measured more precisely than the beam FWHM. We show five examples of our measurements of $R_{\rm min}$ and $V_{\rm max}$ for molecular gas observations in Appendix B. Three examples are from observations that resolve the SOI, and two are from observations that do not. The rest of the measurements are shown in the online supplementary material (PVDs reproduced with permission). Finally, we deproject the observed maximum rotation velocity $V_{\rm max}$ into the maximum circular velocity assuming perfect circular motion and an infinitely thin disc, $V_{\rm c} = V_{\rm max}/\sin(i)$, adopting the inclination and inclination uncertainty listed in each SMBH mass measurement paper.

While there may be non-circular motions or warps in some molecular gas and maser discs, in most cases the errors introduced in $V_{\rm c}$ will be small ($\lesssim$30 km s^{-1}; see e.g. Herrnstein et al. 2005; Nguyen et al. 2020) compared to the large $V_{\rm c}$ in the nuclear regions. These errors are thus unimportant for the following discussion. More complex central non-circular motions (e.g. inflows and/or outflows) associated with bright emission could of course exist in some objects, and they could mimic Keplerian rises of rotation curves due to SMBHs. The galaxy Fairall 49 may be such an example, with faint blueshifted emission near the nucleus explainable by either a Keplerian velocity rise or non-circular motions (Lelli et al. 2022 argued for a molecular gas inflow). Our measurements of $V_{\rm max}$ and $R_{\rm min}$ for this object could thus be more significantly affected.

We thus acknowledge that our measurements of $R_{\rm min}$ and $V_{\rm max}$ of molecular gas observations are only rough estimates with considerable uncertainties. For example, the identification of the velocity peaks is performed visually and may be subject to human biases and uncertainties (e.g. confirmation bias and uncertainties marking the exact location of each peak by hand). Moreover, this method slightly but systematically overestimates $V_{\rm max}$, as it adopts the highest detected velocity, slightly boosted by the velocity dispersion of the gas, rather than the mean of the velocity distribution of the innermost kinematic tracer. We take these effects into account in the adopted uncertainties. For example, we repeat our measurements three times and compare the results to estimate human-related uncertainties. We also ensure that the uncertainty of $V_{\rm max}$ is at least as large as the gas velocity dispersion. The final adopted uncertainties are thus conservative and likely much larger than the systematic uncertainties caused by any of these effects. A more reliable method to measure the $R_{\rm min}$ and $V_{\rm max}$ of molecular gas observations could be to inspect the original data cube of each galaxy and identify the 'innermost detected kinematic tracer' by applying a signal-to-noise ratio threshold. However, we have confirmed using the data cubes of the WISDOM project that these potentially more accurate measurements do not offer a substantial improvement over our more simplistic approach.

3.2 Results

3.2.1 Summary of measured and adopted quantities

Table 1 lists all molecular gas and maser SMBH mass measurements in the literature, as well as our own measurements of $R_{\rm min}$ and $V_{\rm max}$ obtained from those. If a galaxy has multiple SMBH mass measurements from the same method, we consider only the most recent one. All uncertainties listed are 1σ uncertainties. Some inclinations have zero associated uncertainties as they were fixed during the kinematic modelling. If a maser paper does not state an inclination, we assume that the inclination was fixed at 90°, as detection of maser emission requires an almost edge-on maser disc. We added the stellar dynamical mass measurement of Sgr A∗ in the Milky Way (MW) as a reference point, as the motions of individual stars can be measured. The MW $R_{\rm min}$ and $V_{\rm max}$ are taken to be those of the star S2 from GRAVITY Collaboration (2018; hereafter GC18).

If uncertainties are provided, the distances listed in Table 1 are taken from the listed references. Otherwise, we adopt the distances listed in Saglia et al. (2016) and rescale the SMBH masses accordingly (as dynamical mass measurements scale linearly with the assumed distance). If a galaxy is not in Saglia et al. (2016), we adopt a distance from another source, retrieved from the HyperLeda[2] data base (Makarov et al. 2014), and assume a 10 per cent uncertainty, consistent with the approach of van den Bosch (2016).

We also compile the stellar velocity dispersions within one effective radius $\sigma_{\rm e}$ of all the galaxies to compute their $R_{\rm SOI}$. For the MW, we adopt $\sigma_{\rm e} = 105 \pm 20$ km s^{-1} (Gültekin et al. 2009). For other galaxies, we prioritize the $\sigma_{\rm e}$ referenced by the SMBH mass measurement paper. If that paper does not list $\sigma_{\rm e}$, we search the following sources (in descending order of priority):

(i) Sources with well spatially resolved stellar kinematics, such as the ATLAS$^{\rm 3D}$ project (Cappellari et al. 2013) and the MASSIVE survey (Veale et al. 2017). For MASSIVE galaxies, if uncertainties are not provided, we assume 10 km s^{-1}.
(ii) van den Bosch (2016), who compiled the best $\sigma_{\rm e}$ measurements of all galaxies with an SMBH mass measurement before June 2016.
(iii) Other literature sources (e.g. Greene et al. 2010) with $\sigma_{\rm e}$ measurements.
(iv) The 'central stellar velocity dispersion' listed in HyperLeda (Makarov et al. 2014), defined as the mean stellar velocity dispersion within a circular aperture of 0.595 kpc radius.
(v) The 'velocity dispersion' listed in the Sloan Digital Sky Survey (SDSS) data release 16 (DR16; Ahumada et al. 2020), measured within a circular aperture of 1.5 arcsec radius.

We correct the stellar velocity dispersions from HyperLeda and SDSS to $\sigma_{\rm e}$ using $\sigma_{\rm e}/\sigma = (R/R_{\rm e})^{0.08}$ (for spiral galaxies; Falcón-Barroso et al. 2017), where R is the radius of the aperture and σ the corresponding velocity dispersion, and $R_{\rm e}$ is computed from the stellar mass model adopted by the SMBH mass measurement paper. If the galaxy does not have a stellar mass model, we adopt the r-band Petrosian half-light radius from the SDSS DR16 (Ahumada et al. 2020). Because stellar velocity dispersion scales only slowly with aperture size ($\sigma_{\rm e}/\sigma = (R/R_{\rm e})^{\alpha}$, where $-0.06 < \alpha < 0.08$; Falcón-Barroso et al. 2017; Zhu et al. 2023), the differences between σ and $\sigma_{\rm e}$ are unlikely to substantially affect our results. We are unaware of any σ measurement of Fairall 49.

To measure $R_{\rm eq}$, we use the stellar mass model described in each SMBH mass measurement paper. For molecular gas measurements, this usually implies multiplying the best-fitting multi-Gaussian expansion (MGE; Emsellem, Monnet & Bacon 1994; Cappellari 2002) model of the stellar light distribution stated, constructed using the `mge_fit_sectors` procedure of Cappellari (2002), with the corresponding best-fitting mass-to-light ratio (M/L). We then use the

[2]http://leda.univ-lyon1.fr/

`mge_radial_mass` procedure[3] in the JAMPY package[4] (Cappellari 2008, 2020) to convert the two-dimensional stellar mass profile into a one-dimensional radial profile. We interpolate this radial profile to identify the radius $R_{\rm eq}$ at which the enclosed stellar mass equals the best-fitting SMBH mass. Finally, we estimate the uncertainty of $R_{\rm eq}$ using Monte Carlo methods: we recompute $R_{\rm eq}$ using 10^4 random realizations of $M_{\rm BH}$ and M/L sampled from Gaussian distributions with means and standard deviations equal to the best-fitting $M_{\rm BH}$ and M/L and their 1σ uncertainties, respectively. We take the standard deviation of the resultant distribution of $R_{\rm eq}$ as the uncertainty. The $R_{\rm eq}$ of the MW is calculated from the MW nuclear star cluster model of Feldmeier-Krause et al. (2017).

Our procedure to measure $R_{\rm eq}$ is reliable when the adopted stellar mass model comes from an overall dust-free optical or near-infrared image (usually from *HST*) with a resolution comparable to or better than $R_{\rm eq}$. Otherwise, the result will depend strongly on the point spread function and/or the dust distribution model assumed. By checking the Mikulski Archive for Space Telescopes,[5] we confirm that no image satisfies both criteria for any of the maser galaxies in this paper except NGC 4258 (whose model is detailed in Drehmer et al. 2015). The main limitation is that maser galaxies typically have much smaller SOI ($R_{\rm eq} \sim 0.01$ arcsec) than galaxies with molecular gas measurements (see Section 3.2.4). Additionally, the dense molecular gas required to trigger maser emission is often associated with prominent dust, so maser galaxies are typically dusty in their cores. By contrast, all of the SMBH mass measurement papers using molecular gas contain a reliable stellar mass model.

3.2.2 *Sample galaxies in the* M_{BH}–σ_e *diagram*

Fig. 1 shows the correlation of the SMBH masses and the effective stellar velocity dispersions of all galaxies with an SMBH mass measurement using maser or molecular gas kinematics (and the MW), compared to the local $M_{\rm BH}$–$\sigma_{\rm e}$ relation of van den Bosch (2016). Maser observations span an SMBH mass range ($M_{\rm BH} \sim 10^7$ $M_\odot$) much narrower than that of molecular gas observations. The main reason is that the required maser emission originates from a specific type of nuclear activity most frequently present in Seyfert 2 AGNs (see Lo 2005 for a review), with a narrow range of SMBH masses. By contrast, molecular gas observations probe a wide range of galaxy and thus SMBH masses, ranging from massive ellipticals (e.g. Cohn et al. 2021; Smith et al. 2021; Ruffa et al. 2023) to dwarfs (e.g. Davis et al. 2020; Nguyen et al. 2022), constraining SMBH–galaxy scaling relations across the entire dynamic range.

3.2.3 *Comparing* R_{min}/R_{Schw}

Fig. 2 shows the correlation of the radii and the circular velocities of the innermost kinematic tracer measurements of all galaxies with an SMBH mass measurement using maser or molecular gas kinematics (and the MW), in the unit of $R_{\rm Schw}$ and c, respectively. Because $R_{\rm Schw}$ quantifies the physical scales of the motions probed and of processes such as accretion and feedback in the circumnuclear discs, observations with smaller $R_{\rm min}/R_{\rm Schw}$ trace these processes closer to the SMBHs. Using this metric, the best molecular gas SMBH mass measurements resolve spatial scales (i.e. numbers of Schwarzschild

[3]From https://pypi.org/project/mgefit/
[4]From https://pypi.org/project/jampy/
[5]https://mast.stsci.edu/search/ui/#/hst

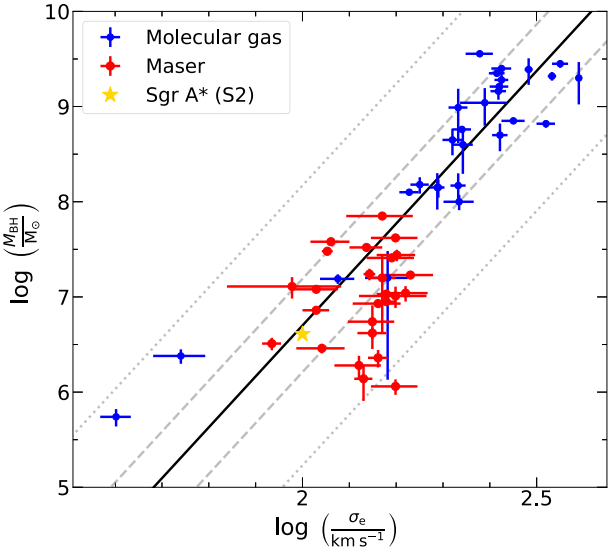

Figure 1. Correlation of the SMBH masses and the effective stellar velocity dispersions of all galaxies with an SMBH mass measurement using maser or molecular gas kinematics (and the MW). The solid black line shows the local $M_{\rm BH}$–$\sigma_{\rm e}$ relation of van den Bosch (2016), while the dashed and dotted grey lines show the 1σ and 3σ observed scatter of the relation, respectively. Maser observations (filled red circles) probe a narrow SMBH mass range ($M_{\rm BH} \sim 10^7$ $M_\odot$), much narrower than that of molecular gas observations (filled blue circles).

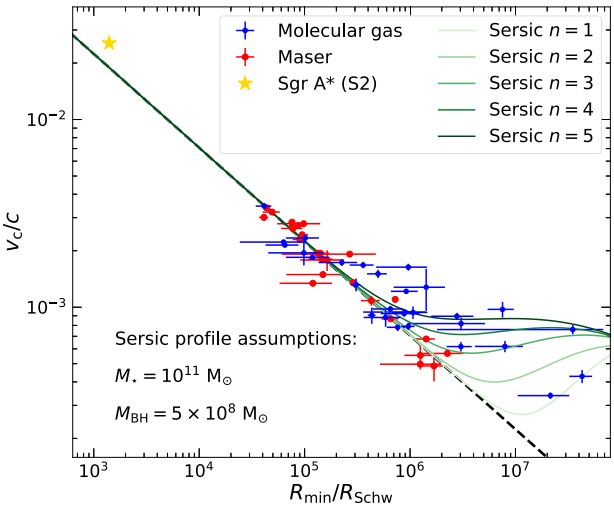

Figure 2. Correlation of the radii and the circular velocities of the innermost kinematic tracer measurements of all galaxies with an SMBH mass measurement using maser or molecular gas kinematics (and the MW), in units of $R_{\rm Schw}$ and c, respectively. The measurement of Sgr A* in the MW uses the peribothron of star S2. The dashed black line shows the Keplerian relation of equation (4). Observations probing fewer Schwarzschild radii from the SMBH tend to follow the Keplerian curve very well, while observations with lower resolutions (in the unit of $R_{\rm Schw}$) deviate from the relation, as the contributions of stars become significant. The expected velocity profiles for a range of Sérsic indices n are shown for comparison as solid curves in different shades of green, for a galaxy with total stellar mass $M_* = 10^{11}$ $M_\odot$ and SMBH mass $M_{\rm BH} = 5 \times 10^8$ $M_\odot$. The best molecular gas SMBH mass measurements resolve spatial scales (i.e. numbers of Schwarzschild radii) comparable to those of the best maser SMBH mass measurements. In fact, the recent high-resolution WISDOM measurement of NGC 383 (leftmost blue data point; Zhang et al. 2024) probes material with smaller $R_{\rm min}/R_{\rm Schw}$ and higher rotational velocities than those of all previous molecular gas *and* maser measurements.

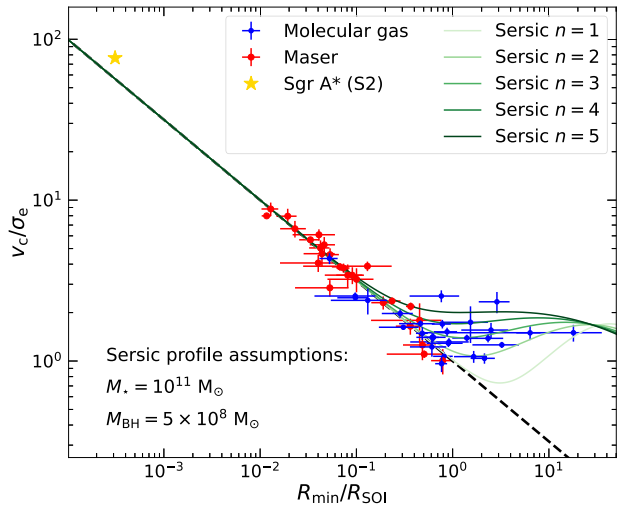

Figure 3. As Fig. 2, but in the unit of $R_{\rm SOI}$ and $\sigma_{\rm e}$, respectively. The $\sigma_{\rm e}$ of each Sérsic profile is derived by first using the `jam_sph_proj` procedure of the JAMPY package to compute the second stellar velocity moment ($V_{*,\rm RMS}$) map and then calculating the luminosity-weighted sum of $V^2_{*,\rm RMS}$ within $R_{\rm e}$. Maser observations generally resolve the SOI better than molecular gas observations. However, the recent high-resolution WISDOM measurement of NGC 383 (leftmost blue data point; Zhang et al. 2024) has a resolution (in the unit of $R_{\rm SOI}$) that is in the same range as that of the best maser observations.

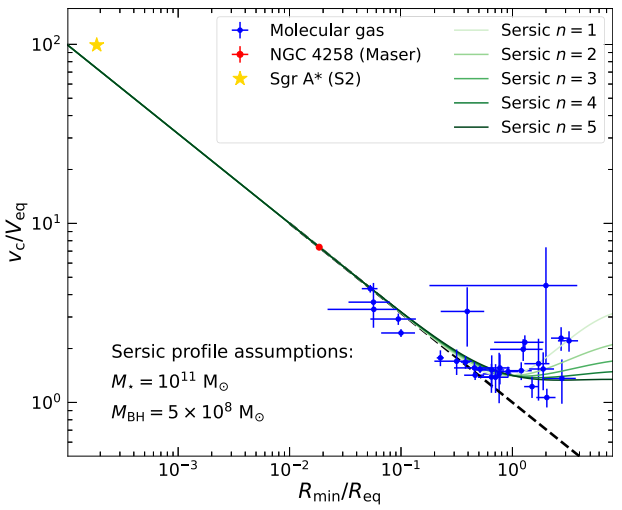

Figure 4. As Fig. 2, but in the unit of $R_{\rm eq}$ and $V_{\rm eq}$, respectively. The only maser galaxy for which we can compute $R_{\rm eq}$ is NGC 4258, which has the largest angular SOI size and the highest resolution SMBH measurement (using either $R_{\rm min}/R_{\rm Schw}$ or $R_{\rm min}/R_{\rm SOI}$ as the metric) of all maser galaxies. So far, molecular gas observations have fewer resolution elements across $R_{\rm eq}$ than the maser observations of NGC 4258, consistent with the results using $R_{\rm SOI}$ as the metric.

radii) comparable to those of the best maser SMBH mass measurements. In fact, the highest resolution (smallest $R_{\rm min}/R_{\rm Schw}$) molecular gas measurement is the recent WISDOM measurement of NGC 383 (Zhang et al. 2024) that probes material with smaller $R_{\rm min}/R_{\rm Schw}$ ($\approx$41 300) and higher $V_{\rm c}$ ($\approx$1040 km s^{-1}) than those of all previous molecular gas *and* maser measurements. This is because, as masers are present in galaxies with SMBH masses typically two orders of magnitude smaller than those of galaxies studied with molecular gas, the poorer angular resolutions of molecular gas observations (compared to those of maser observations) are compensated by the relatively more massive SMBHs probed. Consequently, the highest resolution molecular gas observations can probe physical processes in the circumnuclear discs closer to the SMBHs than maser observations. We note again, however, that this does not guarantee more reliable SMBH mass determinations, as the $R_{\rm min}/R_{\rm Schw}$ metric does not take into consideration the gravitational contributions of stars.

While observations with small $R_{\rm min}/R_{\rm Schw}$ mostly follow the Keplerian velocity profile of equation (4), those with large $R_{\rm min}/R_{\rm Schw}$ tend to deviate from this relation, because the contributions of the stars to the velocity profiles become significant when $R \sim R_{\rm SOI}$. To quantify the typical deviations expected, we generate velocity profiles of a mock galaxy with a total stellar mass $M_* = 10^{11}$ M$_\odot$, an SMBH mass $M_{\rm BH} = 5 \times 10^8$ M$_\odot$, and different Sérsic indices n. This stellar mass is approximately the mid-point of the total stellar mass dynamic range of the galaxies probed with the molecular gas method, and the (M_*, $M_{\rm BH}$) pair adopted is consistent with the M_*–$M_{\rm BH}$ relation of van den Bosch (2016). We note that these parameters are chosen only to illustrate reasonable qualitative trends at large radii, not to reproduce the data points in this region of the diagram. The mass surface density radial profile of the Sérsic model is

$$\Sigma(R) = \Sigma_{\rm e} \exp -b_n \left[\left(\frac{R}{R_{\rm e}} \right)^{1/n} - 1 \right] \ . \tag{12}$$

We estimate the half-light radius $R_{\rm e}$ of each model using the relation of Shen et al. (2003):

$$\frac{R_{\rm e}}{\rm kpc} = \begin{cases} 0.10 \left(\frac{M_*}{\rm M_\odot} \right)^{0.14} \left(1 + \frac{M_*}{3.98 \times 10^{10}\ \rm M_\odot} \right)^{0.25} , & \text{if } n < 2.5 \\ 2.88 \times 10^{-6} \left(\frac{M_*}{\rm M_\odot} \right)^{0.56} , & \text{if } n > 2.5 \ . \end{cases} \tag{13}$$

We approximate b_n as

$$b_n \approx 2\,n - \frac{1}{3} + \frac{4}{405\,n} + \frac{46}{25515\,n^2} \tag{14}$$

(see Ciotti & Bertin 1999), where n is the index of the Sérsic profile. The mass surface density at the effective radius, $\Sigma_{\rm e}$, is normalized by the total stellar mass using

$$M_* = \Sigma_{\rm e} \left(2\pi R_{\rm e}^2 \right) \frac{n\, {\rm e}^{b_n}}{b_n^{2n}} \Gamma(2n) \ , \tag{15}$$

where Γ is the Gamma function. To compute the corresponding three-dimensional mass volume density profiles, we first fit each Sérsic profile with a set of Gaussians (i.e. we perform a MGE fit) using the `mge_fit_1d` procedure of Cappellari (2002). We then use the `mge_vcirc` procedure of the JAMPY package (Cappellari 2008, 2020) to deproject the Gaussians, add an SMBH at the centre, and compute the resulting circular velocity curve. The resulting curves are shown as solid curves with different shades of green in Fig. 2 (with analogous curves in Figs 3 and 4). The data points at large $R_{\rm min}/R_{\rm Schw}$ roughly follow the coloured curves, demonstrating the robustness of our measurements of the innermost tracers.

3.2.4 *Comparing* R_{min}/R_{SOI}

As argued above, detecting material that is fewer Schwarzschild radii away from the SMBH does not in itself guarantee a better SMBH mass measurement, as the measurement precision is more directly related to the factor by which the observations spatially resolve the

SOI. Analogously to Figs 2 and 3 thus shows the correlation of the radii and the circular velocities of the innermost kinematic tracer measurements of all galaxies with an SMBH mass measurement using maser or molecular gas kinematics (and the MW), but this time in the unit of $R_{\rm SOI}$ and $\sigma_{\rm e}$, respectively.

To compute the $\sigma_{\rm e}$ of each Sérsic profile, we adopt the `jam_sph_proj` procedure of the JAMPY package to calculate a prediction of the second stellar velocity moment ($V_{*,\rm RMS}$) from the MGE of the Sérsic profile. Then, we compute $\sigma_{\rm e}^2$ as the luminosity-weighted sum of $V_{*,\rm RMS}^2$ within $R_{\rm e}$. The resulting $\sigma_{\rm e}$ are 110, 111, 122, 126, and 129 $\rm km\,s^{-1}$ for $n = 1$, 2, 3, 4, and 5, respectively.

Again, almost all observations that resolve the SOI ($R_{\rm min}/R_{\rm SOI} < 1$) follow the Keplerian circular velocity curve, while observations with innermost tracers farther from the SMBHs than $R_{\rm SOI}$ are more substantially affected by the galaxies' stellar contents. SMBH mass measurements are nevertheless possible for such observations, if the stellar mass models are sufficiently accurate. In those cases the best-fitting SMBH masses usually have large uncertainties, as the measurements are sensitive to uncertainties in the stellar mass models (and unrealistically small uncertainties would almost certainly imply underestimated systematic uncertainties). So far, all SMBH mass measurements using observations with $R > R_{\rm SOI}$ are measurements with the molecular gas method, as some of the targeted galaxies were revealed to have central holes in their circumnuclear CO(2-1) or CO(3-2) emission (e.g. Davis et al. 2018; Smith et al. 2019, 2021). These holes may imply that the inner edges of the molecular gas discs do not reach the SOI or that the molecular gas within the SOI only emits at higher CO transitions and/or only exists as higher density molecular tracers. In these cases, the radii of the innermost kinematic tracers are greater than $R_{\rm SOI}$ regardless of the angular resolutions of the observations.

The maser observations generally resolve the SOI better than the molecular gas observations, in agreement with the generally better SMBH mass precision they offer. Nevertheless, the highest resolution molecular gas measurement (smallest $R_{\rm min}/R_{\rm SOI}$), again the recent ALMA measurement of NGC 383 (Zhang et al. 2024), has a resolution ($R_{\rm min}/R_{\rm SOI} = 0.05$) that is in the same range as that of the best maser observations. As ALMA's best angular resolution at the frequency of CO(2-1) ($\approx$0.018 arcsec) is about 40 per cent of $R_{\rm min}$ of this measurement, future ALMA molecular gas observations with the most extended configurations can provide comparable $R_{\rm min}/R_{\rm SOI}$ and thus SMBH mass precision as the highest resolution measurements using masers (assuming the observations can achieve sufficient signal-to-noise ratios).

Although the angular resolutions of VLBI maser observations are generally much higher than those of ALMA molecular gas observations, the angular sizes of the SOI of galaxies with maser kinematic SMBH measurements are also usually much smaller than those of galaxies with molecular gas kinematic SMBH measurements, partly because of the smaller $M_{\rm BH}$ of the galaxies with maser emission, and partly because maser-hosting galaxies are on average farther away due to the scarcity of masers. For these reasons, future molecular gas observations with the longest baselines of ALMA can relatively easily achieve the same $R_{\rm min}/R_{\rm SOI}$ as those of the best maser measurements so far. By contrast, megamaser observations have already exploited the highest angular resolution of current facilities (e.g. $\approx$0.35 mas at the frequency of water masers for the Very Long Baseline Array; Napier 1995). It is thus more challenging to improve the precision of SMBH measurements using masers.

3.2.5 *Comparing* R_{min}/R_{eq}

Because $R_{\rm SOI} \equiv GM_{\rm BH}/\sigma_{\rm e}^2$ is only an approximation to the actual SOI radius, we repeat our comparison with $R_{\rm SOI}$ replaced by the equality radius $R_{\rm eq}$, the formal definition of the SOI radius. Fig. 4 thus shows the correlation of the radii and the circular velocities of the innermost kinematic tracer measurements of all galaxies with an SMBH mass measurement using maser or molecular gas kinematics (and the MW), this time in the unit of $R_{\rm eq}$ and $V_{\rm eq}$, respectively. Although only one maser galaxy (NGC 4258) with an SMBH mass determination has an $R_{\rm eq}$ measurement, this galaxy also has the smallest $R_{\rm min}/R_{\rm Schw}$ and $R_{\rm min}/R_{\rm SOI}$ ratios of all maser galaxies, so the maser data point in Fig. 4 represents the best maser observations. These observations still have more resolution elements across the SOI than the molecular gas observations (using $R_{\rm min}/R_{\rm eq}$ as the metric), consistent with the results using the $R_{\rm min}/R_{\rm SOI}$ metric. However, again, ALMA observations with the most extended configurations can relatively easily produce SMBH measurements with a $R_{\rm min}/R_{\rm eq}$ and a precision comparable to the highest resolution measurements using masers.

3.3 Other considerations

In practice, achieving a precise SMBH mass using molecular gas observations requires not only high spatial resolution but also a precise determination of the disc inclination, as the SMBH mass depends strongly on the inclination through the deprojection of the velocities: $M_{\rm BH} \propto \sin^{-2} i$. Due to this $\sin^{-2} i$ dependence, any inclination uncertainty contributes more to the $M_{\rm BH}$ uncertainty budget for smaller (i.e. more face-on) inclinations. As maser discs can only be observed nearly edge-on, inclination uncertainties impact SMBH mass uncertainties less for the maser method than for the molecular gas method.

Another advantage of the maser method is that it sometimes enables an independent galaxy distance determination (e.g. Kuo et al. 2013; Pesce et al. 2020a). As $M_{\rm BH}$ scales linearly with distance, the distance uncertainty often dominates the $M_{\rm BH}$ uncertainty budget, even though it is customary neither to include nor quote the distance uncertainty in other $M_{\rm BH}$ measurements (as rescaling the SMBH mass to a different distance is straightforward and does not require redoing any fit). An independent distance determination using masers thus improves the true SMBH mass precision (including the distance uncertainty), if the distance obtained is more precise than other distance estimates (obtained using e.g. the Tully–Fisher relation; Tully & Fisher 1977).

On the other hand, a clear advantage of the molecular gas method is that it yields truly three-dimensional data and thus a full two-dimensional velocity map of each circumnuclear disc, while the maser method yields effectively one-dimensional kinematics, i.e. the velocities of a few maser spots along the kinematic major axis of the disc only. With many more data points sampling all azimuths, the molecular gas method can provide a reliable SMBH mass even when the data have relatively lower signal-to-noise ratios. Moreover, two-dimensional velocity information allows to properly constrain non-circular motions (e.g. Lelli et al. 2022) and the internal structure of the disc (e.g. warps; Nguyen et al. 2020; Ruffa et al. 2023) that can substantially affect the SMBH mass measurement. Modelling these effects is much more difficult using maser data.

Another advantage of the molecular gas method is that molecular gas observations help constrain the mass distribution of the molecular gas disc itself. An accurate molecular gas mass profile allows to disentangle the dynamical effects of the SMBH from

those of the self-gravity of the molecular gas disc, thus reducing the systematic uncertainty of the SMBH mass measurement. This is especially crucial when the total molecular gas mass within $R_{\rm min}$ is a considerable fraction of the SMBH and/or stellar mass. Measurements with masers, by contrast, require many assumptions to model the disc self-gravity indirectly (e.g. Lodato & Bertin 2003).

4 CONCLUSIONS

The mass of an SMBH can be measured using spectroscopic observations of kinematic tracers at sufficiently small radii, such that the mass enclosed within the tracer's orbit is dominated by the SMBH. Such tracers then follow a Keplerian circular velocity curve, $V_{\rm c} \propto R^{-1/2}$, that can be written in $M_{\rm BH}$-independent forms (equations 4, 7, and 11), affording a fair comparison between SMBH mass measurements that probe different SMBH masses and angular scales. In this paper, we have compared SMBH mass measurements using molecular gas and maser observations, adopting as the metric the radii of their innermost kinematic tracers divided by $R_{\rm Schw}$, $R_{\rm SOI}$, and $R_{\rm eq}$, respectively. We have thus shown that the best molecular gas observations resolve material fewer Schwarzschild radii away from the SMBHs than the best maser observations, so molecular gas observations can probe motions and physical processes closer to the SMBHs than the maser method. Conversely, the best maser observations typically resolve the SMBHs' SOI better than the best molecular gas observations, whether the SOI is defined using the effective stellar velocity dispersion $\sigma_{\rm e}$ or the equality radius $R_{\rm eq}$. Already, molecular gas observations using the most extended configurations of ALMA can spatially resolve the SOI comparably well, leading to SMBH masses as precise as the most precise SMBH masses derived using masers.

If we accept the claim that masers offer 'gold standard' measurements of SMBH masses for $M_{\rm BH} \sim 10^7$ M$_\odot$ (as they resolve the smallest physical scales around the SMBHs), we should consider the molecular gas method capable of producing equally precise measurements across a much wider SMBH mass range. Most of these precise measurements will be towards the high-mass end, where the physical size of the SOI is the largest. Nevertheless, the method can also achieve high precision for a closer, less massive SMBH if a regular and dynamically cold molecular gas disc is present at the centre of the galaxy. Galaxies with lower mass SMBHs are more likely to have turbulent gas kinematics due to the smaller $V_{\rm c}$ and stronger impact of stellar feedback, but regular and circularly rotating CO discs suitable for SMBH mass measurements are also present in some (e.g. Davis et al. 2020). SMBH measurements with molecular gas are thus highly complementary to existing high-precision measurements with masers.

In practice, achieving high angular and thus spatial resolutions requires long baselines and, in turn, long integration times (≈5 h with ALMA). Such observations are not necessarily immediately feasible for a large sample of galaxies. However, the potential for the molecular gas method to steadily increase the number of 'gold standard' mass measurements across the entire SMBH mass range is clear. Moreover, it remains to be seen whether the two methods yield consistent masses for the same galaxies, as no galaxy with an existing SMBH mass measurement from maser observations so far meets the selection criteria for an SMBH measurement using molecular gas (Liang et al. 2024).

ACKNOWLEDGEMENTS

HZ acknowledges support from a Science and Technology Facilities Council (STFC) DPhil studentship under grant ST/X508664/1 and the Balliol College J T Hamilton Scholarship in physics. MB was supported by STFC consolidated grant 'Astrophysics at Oxford' ST/K00106X/1 and ST/W000903/1. IR acknowledges support from STFC grant ST/S00033X/1. This research used observations made with the NASA/ESA *Hubble Space Telescope* and obtained from the Hubble Legacy Archive, which is a collaboration between the Space Telescope Science Institute (STScI/NASA), the Space Telescope European Coordinating Facility (ST-ECF/ESA), and the Canadian Astronomy Data Centre (CADC/NRC/CSA). We acknowledge usage of the HyperLeda data base (http://leda.univ-lyon1.fr).

DATA AVAILABILITY

There is no new datum associated with this article.

REFERENCES

Ahumada R. et al., 2020, ApJS, 249, 3
Barth A. J., Boizelle B. D., Darling J., Baker A. J., Buote D. A., Ho L. C., Walsh J. L., 2016, ApJ, 822, L28
Beifiori A., Courteau S., Corsini E. M., Zhu Y., 2012, MNRAS, 419, 2497
Boizelle B. D., Barth A. J., Walsh J. L., Buote D. A., Baker A. J., Darling J., Ho L. C., 2019, ApJ, 881, 10
Boizelle B. D. et al., 2021, ApJ, 908, 19
Braatz J. A., Wilson A. S., Henkel C., 1996, ApJS, 106, 51
Cappellari M., 2002, MNRAS, 333, 400
Cappellari M., 2008, MNRAS, 390, 71
Cappellari M., 2020, MNRAS, 494, 4819
Cappellari M. et al., 2013, MNRAS, 432, 1862
Ciotti L., Bertin G., 1999, A&A, 352, 447
Cohn J. H. et al., 2021, ApJ, 919, 77
Cohn J. H. et al., 2023, ApJ, 958, 186
Combes F. et al., 2019, A&A, 623, A79
Davis T. A., 2014, MNRAS, 443, 911
Davis T. A., Bureau M., Cappellari M., Sarzi M., Blitz L., 2013, Nature, 494, 328
Davis T. A., Bureau M., Onishi K., Cappellari M., Iguchi S., Sarzi M., 2017, MNRAS, 468, 4675
Davis T. A. et al., 2018, MNRAS, 473, 3818
Davis T. A. et al., 2020, MNRAS, 496, 4061
Dominiak P., Bureau M., Davis T. A., Ma C.-P., Greene J. E., Gu M., 2024a, MNRAS, 529, 1597
Dominiak P. et al., 2024b, preprint (arXiv:2404.11260)
Drehmer D. A., Storchi-Bergmann T., Ferrari F., Cappellari M., Riffel R. A., 2015, MNRAS, 450, 128
Emsellem E., Monnet G., Bacon R., 1994, A&A, 285, 723
Falcón-Barroso J. et al., 2017, A&A, 597, A48
Feldmeier-Krause A., Zhu L., Neumayer N., van de Ven G., de Zeeuw P. T., Schödel R., 2017, MNRAS, 466, 4040
Ferrarese L., Merritt D., 2000, ApJ, 539, L9
GRAVITY Collaboration, 2018, A&A, 615, L15
Gao F. et al., 2017, ApJ, 834, 52
Gebhardt K. et al., 2000, ApJ, 539, L13
Greene J. E. et al., 2010, ApJ, 721, 26
Greenhill L. J., Moran J. M., Herrnstein J. R., 1997, ApJ, 481, L23
Greenhill L. J. et al., 2003, ApJ, 590, 162
Gültekin K. et al., 2009, ApJ, 698, 198
Herrnstein J. R., Moran J. M., Greenhill L. J., Trotter A. S., 2005, ApJ, 629, 719
Kabasares K. M. et al., 2022, ApJ, 934, 162
Kabasares K. M. et al., 2024, preprint (arXiv:2403.00181)
Kondratko P. T., Greenhill L. J., Moran J. M., 2008, ApJ, 678, 87

Kormendy J., Ho L. C., 2013, ARA&A, 51, 511
Krajnović D., Cappellari M., McDermid R. M., 2018, MNRAS, 473, 5237
Kuo C. Y. et al., 2011, ApJ, 727, 20
Kuo C. Y., Braatz J. A., Reid M. J., Lo K. Y., Condon J. J., Impellizzeri C. M. V., Henkel C., 2013, ApJ, 767, 155
Kuo C. Y. et al., 2020, MNRAS, 498, 1609
Lelli F., Davis T. A., Bureau M., Cappellari M., Liu L., Ruffa I., Smith M. D., Williams T. G., 2022, MNRAS, 516, 4066
Liang F.-H. et al., 2024, MNRAS, 527, 9343
Lo K. Y., 2005, ARA&A, 43, 625
Lodato G., Bertin G., 2003, A&A, 398, 517
Magorrian J. et al., 1998, AJ, 115, 2285
Makarov D., Prugniel P., Terekhova N., Courtois H., Vauglin I., 2014, A&A, 570, A13
Mamyoda K., Nakai N., Yamauchi A., Diamond P., Huré J.-M., 2009, PASJ, 61, 1143
Nagai H. et al., 2019, ApJ, 883, 193
Napier P., 1995, in Zensus J. A., Diamond P. J., Napier P. J., eds, ASP Conf. Ser. Vol. 82, Very Long Baseline Interferometry and the VLBA. Astron. Soc. Pac., San Francisco, p. 59
Nguyen D. D. et al., 2020, ApJ, 892, 68
Nguyen D. D. et al., 2021, MNRAS, 504, 4123
Nguyen D. D. et al., 2022, MNRAS, 509, 2920
North E. V. et al., 2019, MNRAS, 490, 319
Onishi K., Iguchi S., Sheth K., Kohno K., 2015, ApJ, 806, 39
Onishi K., Iguchi S., Davis T. A., Bureau M., Cappellari M., Sarzi M., Blitz L., 2017, MNRAS, 468, 4663
Pesce D. W. et al., 2020a, ApJ, 890, 118
Pesce D. W. et al., 2020b, ApJ, 891, L1
Rohatgi A., 2022, Webplotdigitizer: Version 4.6. https://automeris.io/WebPlotDigitizer
Ruffa I. et al., 2019, MNRAS, 489, 3739
Ruffa I. et al., 2023, MNRAS, 522, 6170
Saglia R. P. et al., 2016, ApJ, 818, 47
Sahu N., Graham A. W., Davis B. L., 2019, ApJ, 887, 10
Schwarzschild K., 1916, Sitzungsberichte der Königlich Preussischen Akademie der Wissenschaften, 67, 189
Shen S., Mo H. J., White S. D. M., Blanton M. R., Kauffmann G., Voges W., Brinkmann J., Csabai I., 2003, MNRAS, 343, 978
Simmons B. D., Smethurst R. J., Lintott C., 2017, MNRAS, 470, 1559
Smith M. D. et al., 2019, MNRAS, 485, 4359
Smith M. D. et al., 2021, MNRAS, 503, 5984
Tully R. B., Fisher J. R., 1977, A&A, 54, 661
van den Bosch R. C. E., 2016, ApJ, 831, 134
Veale M. et al., 2017, MNRAS, 464, 356
Wolfe A. M., Burbidge G. R., 1970, ApJ, 161, 419
Yamauchi A., Nakai N., Sato N., Diamond P., 2004, PASJ, 56, 605
Yamauchi A., Nakai N., Ishihara Y., Diamond P., Sato N., 2012, PASJ, 64, 103
Zhang H. et al., 2024, MNRAS, submitted
Zhao W. et al., 2018, ApJ, 854, 124
Zhu K., Lu S., Cappellari M., Li R., Mao S., Gao L., Ge J., 2024, MNRAS, 527, 706

SUPPORTING INFORMATION

Supplementary data are available at *MNRAS* online.
Please note: Oxford University Press is not responsible for the content or functionality of any supporting materials supplied by the authors. Any queries (other than missing material) should be directed to the corresponding author for the article.

APPENDIX A: SUMMARY OF AS YET UNPUBLISHED SMBH MASS MEASUREMENTS

This appendix summarizes two submitted but as yet unpublished SMBH mass measurements from the WISDOM project.

A1 NGC 383

The SMBH mass of the nearby lenticular galaxy NGC 383 is measured by Zhang et al. (2024) using ALMA observations of the ^{12}CO(2-1) emission line with a synthesized beam FWHM of $\approx 16 \times 8$ pc^2 (0.051 arcsec $\times$ 0.025 arcsec). This angular (and thus spatial) resolution is approximately four times better than that of the previous intermediate-resolution measurement by North et al. (2019) and it spatially resolves the SOI by a factor of $\approx$23. The observations yield $V_{\rm max} \approx 634$ km s^{-1} (corresponding to a deprojected velocity $V_{\rm c} \approx 1040$ km s^{-1}), $\approx$1.8 times higher than that of North et al. (2019), as well as evidence for a mild position angle warp and/or non-circular motions within the central $\approx$0.3 arcsec. By forward modelling the mass distribution and ALMA data cube, Zhang et al. (2024) infer an SMBH mass of $(3.59 \pm 0.20) \times 10^9$ M$_\odot$ (1σ confidence interval), more precise (5 per cent) but consistent with ($\approx 1.4\sigma$ smaller than) the measurement by North et al. (2019). The best-fitting SMBH mass is insensitive to varying models of the central warp and/or non-circular motions. The PVD of the ALMA data, overlaid with that of the best-fitting model, is shown in the online supplementary material.

A2 NGC 4751

The SMBH mass of the ETG NGC 4751 is measured by Dominiak et al. (2024b) using ALMA observations of the ^{12}CO(3–2) line with an angular resolution of $\approx$24 pc (0.19 arcsec). The observations reveal a regularly rotating central molecular gas disc with clear central Keplerian motions. By forward modelling the molecular gas kinematics and data cube, Dominiak et al. (2024b) infer an SMBH mass $M_{\rm BH} = 3.43^{+0.45}_{-0.44} \times 10^9$ M$_\odot$ assuming a constant stellar M/L, but an SMBH mass $M_{\rm BH} = 2.79^{+0.75}_{-0.57} \times 10^9$ M$_\odot$ assuming a linearly spatially varying M/L. We adopt the linearly varying M/L model as it agrees more closely with the SMBH mass derived through stellar kinematics in the same paper. The PVD of the ALMA data, overlaid with that of the best-fitting linearly varying M/L model, is shown in the online supplementary material.

APPENDIX B: EXAMPLES OF INNERMOST TRACER MEASUREMENTS OF MOLECULAR GAS OBSERVATIONS

Figs B1–B5 show five examples of our measurements of the innermost kinematic tracers used for SMBH mass measurements with the molecular gas method. The first three examples are from observations that spatially resolve the SOI. The last two examples are from observations that do not detect emitting material within the SOI due to a central hole in the CO(2-1) morphology. Similar figures for all remaining measurements are shown in the online supplementary material.

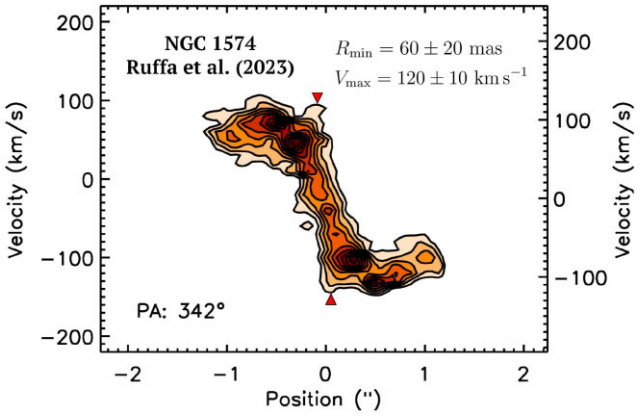

Figure B1. Major-axis PVD of the CO(2-1) emission of the galaxy NGC 1574 (fig. 5d of Ruffa et al. 2023). The red triangles indicate the data points we adopt as the innermost kinematic tracer.

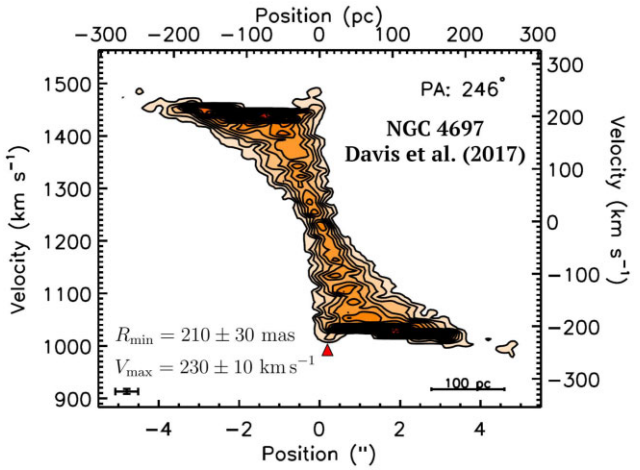

Figure B2. As Fig. B1 but for the galaxy NGC 4697 (fig. 2 of Davis et al. 2017). The emission at the highest positive velocity may well be noise, so we choose not to take our measurement there.

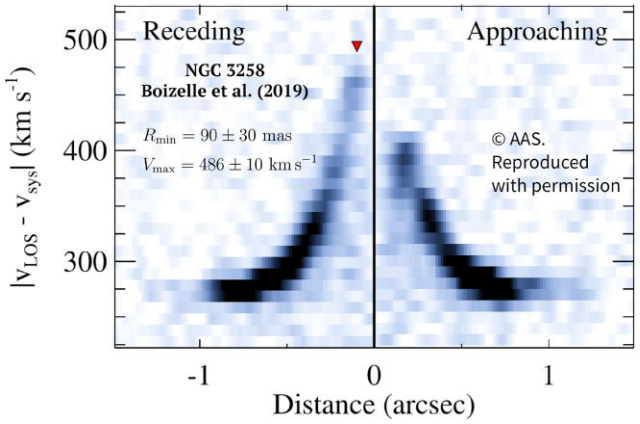

Figure B3. As Fig. B1 but for the galaxy NGC 3258 (fig. 5 of Boizelle et al. 2019). As the redshifted and the blueshifted velocity peaks are strongly asymmetric, we adopt only the higher velocity peak.

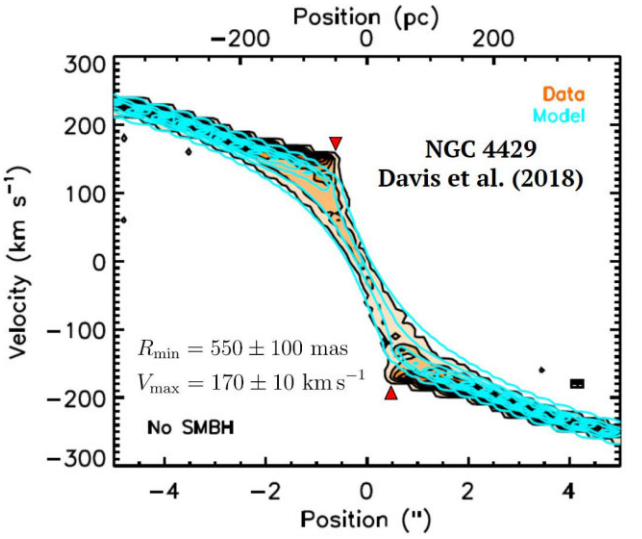

Figure B4. As Fig. B1 but for the galaxy NGC 4429 (fig. 10 of Davis et al. 2018). Although there is no central rise in velocity, we identify the innermost kinematic tracer as the innermost point before the velocity falls off rapidly to zero. The innermost kinematic tracer is outside the SMBH SOI because of a central hole in the CO(2-1) morphology. Yet, an SMBH mass measurement is possible as the velocity of the tracer is higher than that expected from the best-fitting model without an SMBH (cyan contours).

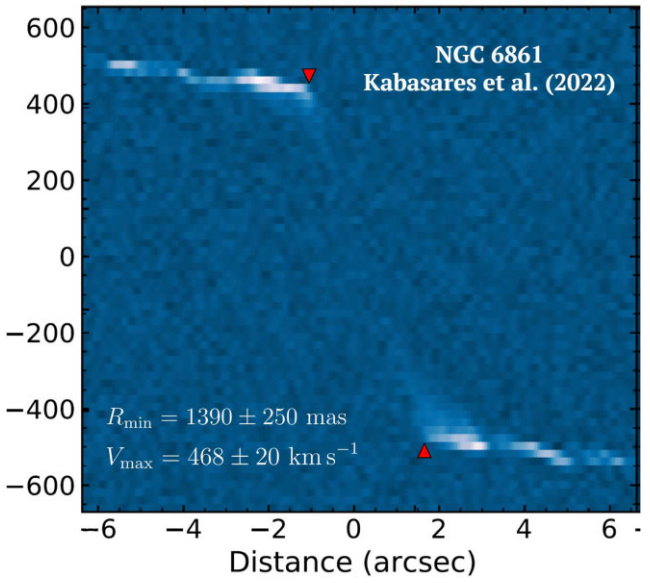

Figure B5. As Fig. B1 but for the galaxy NGC 6861 (fig. 7 of Kabasares et al. 2022). The PVD was plotted using a continuous colour map without contours, so we visually identify the innermost point that is distinguishable from noise.

This paper has been typeset from a TEX/LATEX file prepared by the author.